Structural, spectral, dielectric, and magnetic properties of Ca–Ba-substituted $Sr_2Ni_2Fe_{28}O_{46}$ X-type hexaferrites

Syeda Rabia Ejaz[1,2] · **Muhammad Azhar Khan**[2] · **Shagufta Gulbadan**[2] · **Muhammad Shahzad Shifa**[2] · **Ghulam Murtaza**[3]

Abstract

Nanocrystalline X-type hexaferrites having the chemical composition of $Sr_{2-x}Ca_xNi_{2-y}Ba_yFe_{28}O_{46}$ ($x = y = 0$–0.5) were synthesized via sol–gel auto-combustion route at a sintering temperature of 1250 ˚C for 5 h. XRD analysis was done to verify the hexagonal X-type structure. All peaks were indexed according to the standard card of X-type ferrite. The increase in XRD parameters (a, c) and cell volume was observed by increasing the Ca–Ba substitution. Scherrer's equation unfolded the crystalline size (22.97–26.61 nm). The inclusion of Ca–Ba significantly altered the porosity and X-ray density of synthesized materials. Infrared spectra revealed crystal symmetry in agreement with XRD analysis. The Ac conductivity was enhanced by systematically substituting Ca–Ba from (1.453×10^{-5} to 7.048×10^{-5}) Ωcm^{-1}. The complex impedance inspection of synthesized composition shows the promising part of grain boundaries involvement to the dielectric properties. The dielectric constant values of all synthesized compositions were greater than $Sr_2Ni_2Fe_{28}O_{46}$, making these materials interesting for use in many applications requiring a high dielectric constant. Vibrating sample magnetometer analysis (VSM) was utilized to observe the magnetic characteristics. The magnetic properties were decreased with the inclusion of Ca–Ba cations concentration. The low values of the coercivity of this synthesized X-type hexagonal ferrite suggest using this material for memory devices, microwave absorption, and magnetic radar-absorbing materials used in high-frequency applications.

Keywords Structural analysis · Cole–Cole plot · Remanence · Coercivity · Anisotropy constant

1 Introduction

Nowadays, the synthesis of nanomaterials is of great attention due to their uniqueness and relatively remarkable properties. These attractive properties allow these nanomaterials to be employed in novel applications in science and technology. Ferrites are vital materials for technological applications [1]. Ferrites exist in the different crystalline structures like spinel, ortho- ferrites, hexagonal, and garnet. Ferrites

are the most significant magnetic materials because of having low cost, good chemical stability, and extensive technical applications in the transformer core, high-quality filters, and recording media [2]. Out of these, hexagonal ferrites are a significant class of magnetic material. Hexagonal ferrites are hard ferrite materials that have been frequently used in various industrial and technological fields [3]. These materials have the potential for microwave applications due to the following characteristics: excellent oxidation resistance, the high value of coercivity, remanence, and magnetic energy products. These materials are considered valuable to microwave applications [4].

Depending upon their crystal configuration, there are seven possible hexagonal ferrites differentiated as X, Y, M, Z, W, U, and R [5]. Among various hexagonal structures, X-type hexagonal ferrites represented by the formula "$Ba_2Me_2Fe_{28}O_{46}$" (Me is a divalent ion) were first reported in 1952. The X-type hexagonal ferrites are regarded as an attractive material because of their prospective relevance as the permanent magnets used for microwave devices [6].

✉ Syeda Rabia Ejaz
  rabia.ejaz@gscwu.edu.pk

✉ Muhammad Azhar Khan
  azhar.khan@iub.edu.pk

1 Department of Physics, The Government Sadiq College Women University Bahawalpur, Bahawalpur 63100, Pakistan

2 Institute of Physics, The Islamia University of Bahawalpur, Bahawalpur 63100, Pakistan

3 Department of Physics, G. C. University, Lahore 54000, Pakistan

The basic configuration of X-type hexaferrite consists of S and R blocks along the central axis, having a stacking representation as RSR*S*S*(* indicates alternation of the analogous block by 180° about the c-axis) [7]. Three octahedral sites are present at the border between S and R and S–S blocks. Two tetrahedral and one octahedral site are in the "S" block. One trigonal bipyramidal and two octahedral sites are located in the R block [8]. X-type ferrites are ferrimagnetic [9] material formed by the combined phase of W-type and M-type hexagonal ferrites [10]. Various techniques have been used to synthesize the X-type hexagonal ferrites. Few are the micro-emulsion method, sol–gel process, and co-precipitation route [11]. Among these synthesis routes, sol–gel auto-combustion has been found extremely interesting because it can suitably utilize heat released from the in-situ reactions of the chemicals, such as from the chelating agents and the nitrate radicals. Sol–gel technique was first employed to synthesize X-type hexagonal ferrites by Pullar et al. to prepare Co_2 substituted X-type hexagonal ferrites [12]. Haijun, Z. et al. discussed $Ba_2Zn_2Fe_{28}O_{46}$ hexaferrites restraining a thin ferromagnetic resonance linewidth and discussed the significant aspects that influence the properties of metal substituted hexaferrites are choice of suitable dopants and preparation routes to perform multiplicity applications [13].

Hence, the magnetic, dielectric, and structural assets of X-type hexaferrites are dependent on many factors, including the chemical composition, synthesis methodology, sintering temperature, and sintering time. In the current work, the principal purpose of the investigation is to explore the consequence of Ca^{2+}–Ba^{2+} substitution for Sr^{2+}–Ni^{2+} in $Sr_2Ni_2Fe_{28}O_{46}$ X-type ferrite prepared via auto-combustion sol–gel method.

This effort aims to understand the influence of Ca^{2+}–Ba^{2+} of substitutions on structural, spectral, magnetic, and dielectric parameters. Literature evidenced that phases of the compositions and dielectric parameters may be altered via control by choosing the substitution of the various divalent and trivalent cations at the different sites of the hexagonal lattice. Therefore, tailoring the composition makes it possible to improve the properties essential for the particular application.

2 Experimental procedure

2.1 Chemicals

Chemical used for the fabrication of $Sr_{2-x}Ca_xNi_{2-y}Ba_yFe_{28}O_{46}$ ($x = y = 0$–0.5) composition were $Sr(NO_3)_2$, $Ni(NO_3)_2.H_2O$, $Ca(NO_3)_2$, $Ba(NO_3)_2$ and $Fe(NO_3)_3.9H_2O$.

2.2 Synthesis methodology

Ca–Ba-substituted X-type hexagonal ferrites with composition $Sr_{2-x}Ca_xNi_{2-y}Ba_yFe_{28}O_{46}$ ($x = y = 0$–0.5) was prepared by sol–gel auto-combustion route. The appropriate amount of metal nitrates solutions was prepared by dissolving the salts in the water (deionized). After preparing the homogeneous solution, mix the appropriate amount of the desired solution according to the composition. The molar ratio of the metal nitrate relative to the citric acid was 1:1. The citric acid solution was added to the metal nitrate solutions with continuous stirring at 40 ℃. $C_6H_8O_7$ serves as a chelating agent that assists the homogeneous distribution of the metal ions. Ammonium hydroxide was drop-wise added to the solution with constant stirring to control pH at 7. After maintaining pH, the solution was stirred at a steady temperature until water evaporation occurred, resulting in viscous gel formation. The so attained viscous gel was further heated at 150 ℃, leads to the ignition of gel, and the fluffy dry residue was received as shown in Fig. 1. The fluffy powder was crushed in an agate mortar pestle to get the fine particles and then sintered at 1250 ℃ for 5 h in a muffle furnace. After annealing, the powder was ground to obtain a fine powder.

2.3 Characterization

The un-annealed material was characterized via thermal gravimetric analysis and differential thermal analysis (Model: Mettler toledo Gc 200) at a temperature of 10 ℃ / min from room temperature to 1300 ℃. After the heating treatment, the phase recognition was verified by a Bruker X-ray diffractometer using a Cu-kα_1 radiation source. FTIR spectroscopy was utilized to explore the spectral information in 400–1000 cm^{-1}. The impedance analyzer and vibrating sample magnetometer explored dielectric measurements and magnetic properties.

3 Results and discussion

3.1 Thermal analysis

To explore the structure development process of $Sr_{2-x}Ca_xNi_{2-y}Ba_yFe_{28}O_{46}$ composition, TGA, DTGA, and DSC were used to determine the decomposition procedure of as-synthesized composition. Figure 2 shows the TGA, DTGA, and DSC curves in the temperature range of 0 to 1300 °C. The plot of TDA shows five weight loss regions: At a temperature of 170 °C, the initial weight loss peaks as a result of the evaporation of water molecules among the voids of particles. At a temperature of 415 °C, the second peak,

Fig. 1 The formation stages of the synthesized composition using sol–gel auto-combustion route
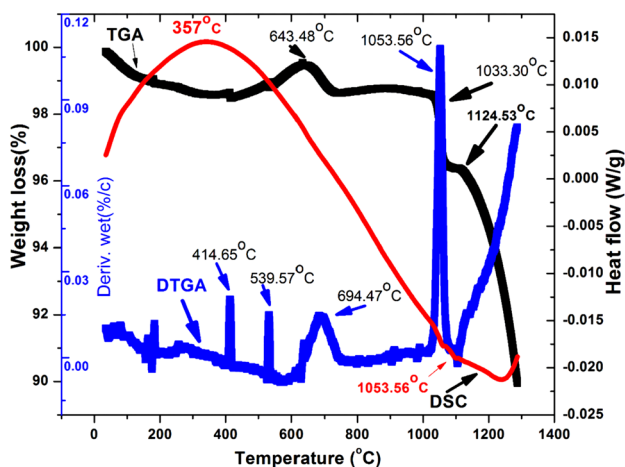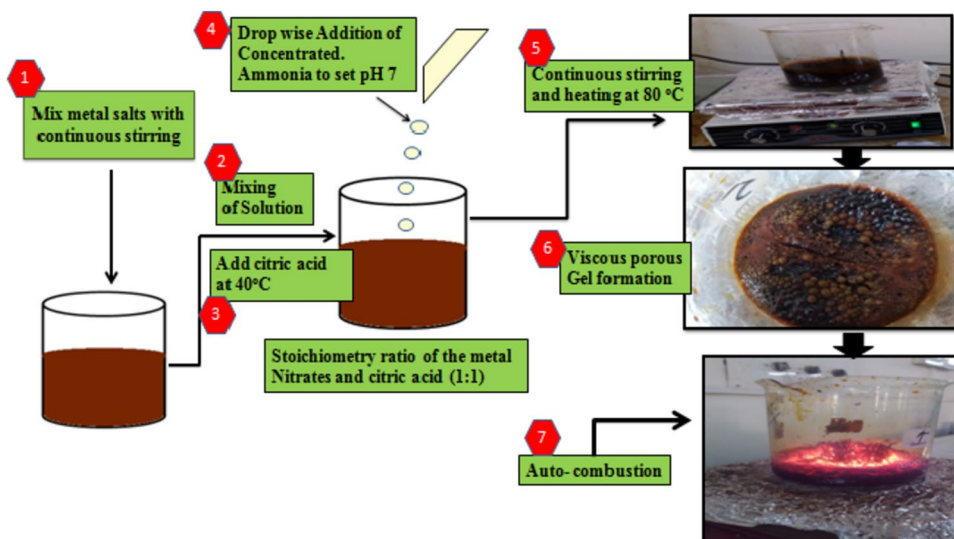

Fig. 2 TGA, DSC and DTGA plots of $Sr_2Ni_2Fe_{28}O_{46}$ powder sample

which was caused by the release of trapped water or the crystallization of water, appears. The other weight loss peak emerges at 643.480 °C, which might be explained by the elimination of organic components, breakdown of nitrates, citric acid, and the configuration of metal oxide. The transformation of hydroxide to oxides is what causes the weight loss that was noticed at this temperature. The growth of the hexagonal structure is responsible for the weight loss that occurred after 1000 °C and the smoothed line that appeared within regions between 1033 °C and 1124.53 °C.[14, 15]. The temperature greater than 1124.53 °C did not cause any weight loss [8, 16].

In the DTGA, an exothermic peak observed at different temperatures was observed. The exothermic peaks observed at 414.65 °C, 539.57 °C are the indication of removal of water molecules and nitrates from the sample, while peaks at 694.47 °C,1053.56 °C correspond to the burning of the

organic components and the development of the hexagonal phase, respectively [17]. Exothermal and endothermal peaks were seen in the DTGA curve between 30 and 695 °C, confirming the TGA findings. The other endothermal peak was likewise seen at 1200 °C, demonstrating the phase's development. DSC curve gives two endothermic peaks. A wide peak was found in the DSC curve at 357 °C, confirming the TGA curve's indication of the sample's greatest weight loss. This peak (at ∼357 °C) is due to the evolution of the gases, and also ascribed to the removal of absorbed water. The second peak observed at 1053.56 °C is because of the emergence of X-type hexagonal phase [18]. Hence, it was established from all of these investigations that the synthesized materials are quite stable above 1200 °C. Consequently, the synthesized material was sintered at 1250 °C to achieve the necessary phase [19].

3.2 Phase identification

XRD patterns of all prepared X-type hexaferrites compositions are demonstrated in Fig. 3. The obtained patterns of $Sr_{2-x}Ca_xNi_{2-y}Ba_yFe_{28}O_{46}$ X-type hexagonal ferrites are indexed with the standard pattern (ICDD#01–079-0476). The intense peaks are well indexed as (110), (0126) (1115), (205), (2011), (0222), (0228), (2110), (306), (1226), (0315), (220), (1313) and (1325). The entire synthesized sample exhibited no extra peak, indicating no impurity phase formed during sintering which confirmed the single-phase formation of X-type. It can be seen from the graph that maximum reflection is at $2\theta = 34.28$ and showed good accord with the earlier data reported in the literature for the X-type [20, 21].

Lattice parameters are found by cell software. Table 1 depicts the values of lattice parameters, X-ray density, porosity, cell volume, bulk density, and c/a ratio of different Ca^{2+}-Ba^{2+} substitution compositions in $Sr_2Ni_2Fe_{28}O_{46}$
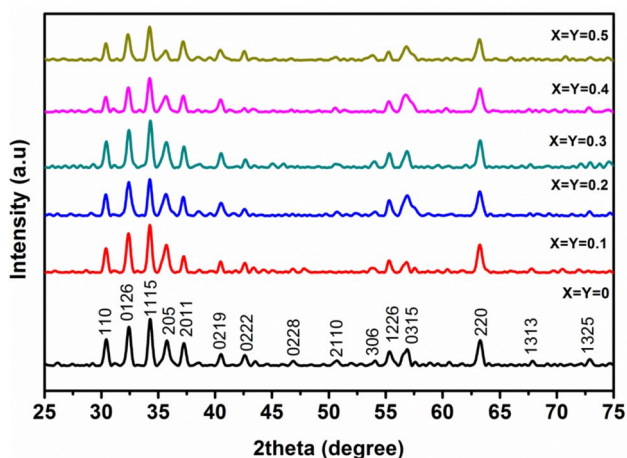
Fig. 3 XRD patterns of $Sr_{2-x}Ca_xNi_{2-y}Ba_yFe_{28}O_{46}$ ($x=y=0$, 0.1, 0.2, 0.3, 0.4, 0.5) X-type hexaferrites

X-type ferrite. The increasing trend in the lattice constants was observed with increasing fractions of cations, i.e., Ca–Ba. The discrepancy in lattice parameters might be accredited to the more enormous ionic radii of Ba^{2+} (1.35 Å) concerning Ni^{2+} (0.72 Å) ion. The c/a ratio falls in 14.24 ranges in the entire prepared ferrites, indicating that the material lies in X-type hexagonal ferrites. The unit volume cell, X-ray density, porosity, and bulk density were obtained by the relations (1–4) [22].

$$V = a^2c \sin 120°, \tag{1}$$

$$\delta_m = \frac{m\pi}{r^2h}, \tag{2}$$

$$\delta_X = \frac{ZM}{N_AV}, \tag{3}$$

$$P = 1 - \delta_m\delta X. \tag{4}$$

The cell volume increases from 2519.97 to 2531.79 Å^3 and is justified based on lattice parameters [23]. As the

average ionic radius of Ba^{2+} (1.49 Å) and Ca^{2+} (1.06 Å) are greater than Ni^{2+} (0.72 Å) and Sr^{2+} (1.13 Å) causes the enlargement of lattice parameters as well the unit cell volume enhancement [24, 25]. It is also examined from Table 1 that the X-rays density and bulk density increase by the increase in the substitution of Ca^{2+}–Ba^{2+}. This behavior is accredited due to the discrepancy in the molar masses of the host and the substituted ions. The observed value of the bulk density is lesser than the X-ray's density owing to the existence of inevitable pores formed during the annealing [26]. The difference in X-ray density by varying substitution plays a significant role in deciding the porosity. It is also reported that porosity is dependent upon many factors such as density, crystalline size, annealing temperature, and preparation technique. Table 1 illustrates the decrease in the porosity was noticed through the increase in the Ca^{2+}–Ba^{2+} substitution. The crystalline size was found in the range of 22.97–26.61 nm.

The interchange distance (r), strain (η), distortion parameter (g), and the dislocation density (δ) were determined. The Wilson evaluated the strain of the nanoparticle ferrites–stokes formula [27] $\eta = (\beta/4)\tan\theta$ and the g, δ r [28] were computed by the Eqs. 5–7.

$$r = 5\lambda/8\sin\theta, \tag{5}$$

$$\delta = \frac{1}{D2}, \tag{6}$$

$$g = \beta/\tan\theta. \tag{7}$$

A decrease in the interchange distance is observed with an increase in the Ca–Ba concentration. However, the intensity and crystalline size decrease can explain the reduction in the interchange length. Deviation of "δ" and g is a consequence of the site vacancies' existence in the crystal layers and the re-ordering of atoms in the lattice. It can be noticed from Table 2 that the crystalline size increases, whereas the strain and dislocation density decreases. This parameter variation could affect the re-crystallization progression in the prepared composition.

Table 1 The structural parameters of $Sr_{2-x}Ca_xNi_{2-y}Ba_yFe_{28}O_{46}$

Ca–Ba contents	a(Å)	c(Å)	c/a	V(Å)^3	D (nm)	δ_x (g/cm^3)	δ_b (g/cm^3)	Porosity
$x=0, y=0$	5.890	83.878	14.24	2519.97	22.97	5.123	2.739	0.4653
$x=0.1$ $y=0.1$	5.893	83.950	14.25	2524.98	25.23	5.119	2.944	0.4249
$x=0.2, y=0.2$	5.896	83.941	14.23	2526.66	25.98	5.122	3.114	0.3920
$x=0.3, y=0.3$	5.889	83.902	14.25	2520.0	24.48	5.142	2.951	0.4261
$x=0.4, y=0.4$	5.897	83.933	14.23	2528.23	26.61	5.132	2.899	0.4350
$x=0.5, y=0.5$	5.899	83.994	14.23	2531.79	24.73	5.130	3.530	0.3119

Table 2 Structurally extracted parameters of $Ba_{2-x}Mg_xCo_{2-y}Sr_y$ $Fe_{28}O_{46}$

Ca–Ba contents	Dislocation Density (lines\m^{-2})	Interchange distance (nm)	Distortion parameter	Micro-Strain
$x=0, y=0$	1.9×10^{15}	3.2658	1.00599	2.392×10^{-2}
$x=0.1\ y=0.1$	1.57×10^{15}	3.2677	9.0356×10^{-1}	2.181×10^{-2}
$x=0.2, y=0.2$	1.48×10^{15}	3.2677	8.7564×10^{-1}	2.114×10^{-2}
$x=0.3, y=0.3$	1.67×10^{15}	3.2639	9.3894×10^{-1}	2.236×10^{-2}
$x=0.4, y=0.4$	1.41×10^{15}	3.2696	8.6103×10^{-1}	2.042×10^{-2}
$x=0.5, y=0.5$	1.64×10^{15}	3.2728	9.6467×10^{-1}	2.283×10^{-2}
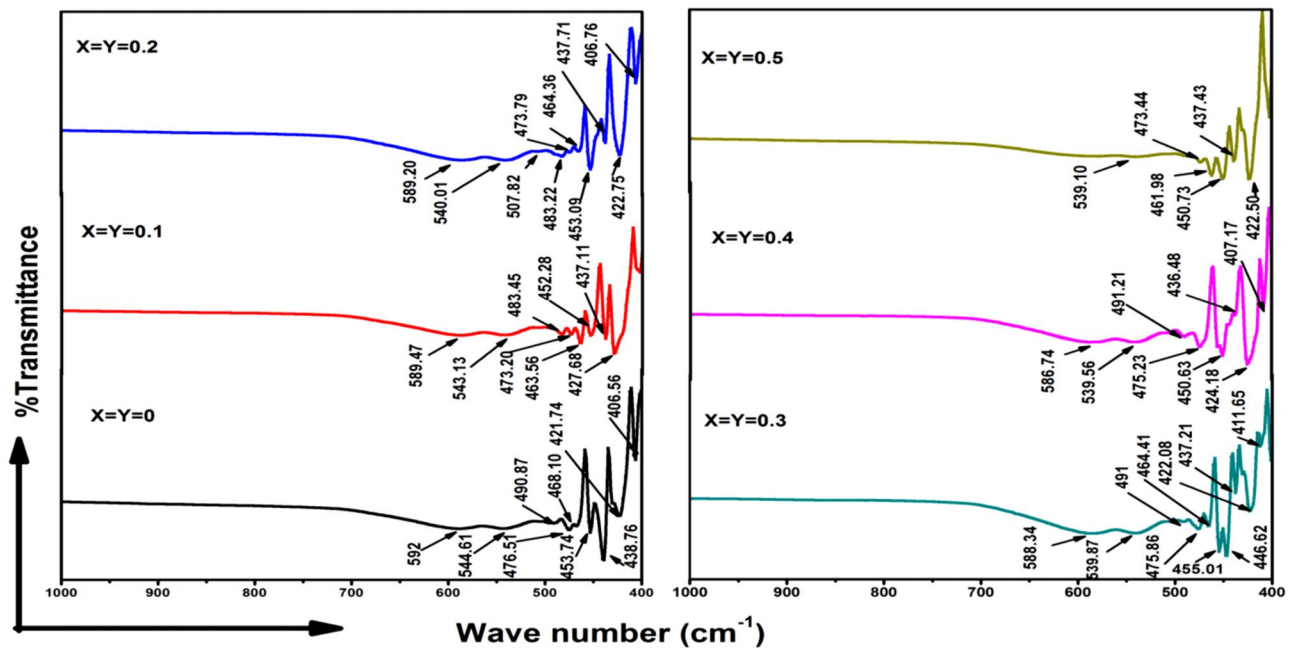
Fig. 4 FTIR spectra of $Sr_{2-x}Ca_xNi_{2-y}Ba_yFe_{28}O_{46}$ ($x=y=0$, 0.1, 0.2, 0.3, 0.4, 0.5) X-type hexaferrites

3.3 FTIR analysis

Figure 4 illustrates the FTIR spectra of annealed $Sr_{2-x}Ca_xNi_{2-y}Ba_yFe_{28}O_{46}$ X-type Hexa ferrites in 400–1000 cm^{-1}. The entire composition spectra showed the absorption bands in 438–540 cm^{-1}. These characteristic bands are ascribed to intrinsic vibrations of the octahedral (υ_2) and tetrahedral (υ_1) metal–oxygen bonds, respectively [29].

In the present work, absorption bands in the range of 438.76–436.48 cm^{-1} (υ_2) correspond to the task of Fe–O stretching through Fe–O$_6$, while the bands occur in 544.61–539.10 cm^{-1} (υ_1) due to the Fe–O stretching of Fe–O$_4$ [30]. It can be observed from the spectra that for $Sr_2Ni_2Fe_{28}O_{46}$ composition, octahedral (υ_2) and tetrahedral (υ_1) bands are located at 438.76 cm^{-1} and 544.61 cm^{-1}, respectively. It reveals the band's location variation with the enhancement of substitution. A slight deviation in the location of the bands in

all synthesized material is predicted. This might be due to the dissimilarity between tetrahedral (A) and octahedral (B) ions. The variations in υ_1 and υ_2 with Ca–Ba substitution are given in Table 3. The values of υ_1 and υ_2 are decreasing towards lower wavenumber with the increase in Ca–Ba substitution. It can be justified based on the allocation of the cations on tetrahedral and octahedral sites [31].

The band shifting as a function of Ca–Ba substitution and force constants of octahedral K_o and tetrahedral K_t can be measured using the formulae (8–9). It was observed that K_o and K_t showed decreasing behavior with the increasing Ca–Ba contents. The tetrahedral clusters' vibrational mode is greater than that of the octahedral clusters due to the shorter bond length of the tetrahedral clusters.

$$K_o\left(dynes\ cm^{-2}\right) = 0.942128 * M\upsilon_2^2/(M+32), \qquad (8)$$

Table 3 Spectral parameters of $Sr_{2-x}Ca_xNi_{2-y}Ba_yFe_{28}O_{46}$

Ca–Ba contents	υ_1 (cm^{-1})	υ_2 (cm^{-1})	Molecular weight (g/mol)	K_o (dynes cm^{-2})*10^5	K_t (dynes cm^{-2})*10^5	Bond length (Å)
$x=0,y=0$	544.61	438.76	2592.246	1.792	3.145	21.107
$x=0.1$ $y=0.1$	543.13	437.11	2595.355	1.778	3.125	21.125
$x=0.2,y=0.2$	540.01	437.71	2598.464	1.783	3.111	21.123
$x=0.3,y=0.3$	539.87	437.21	2601.574	1.779	3.107	21.113
$x=0.4,y=0.4$	539.56	436.48	2604.683	1.773	3.099	21.121
$x=0.5,y=0.5$	539.10	437.43	2607.792	1.781	3.104	21.136

$$K_t\left(\text{dynes cm}^{-2}\right) = 2^{1/2}K_o\upsilon_1/\upsilon_2. \tag{9}$$

The bond length of the hexagonal structure is determined using the Eqs. 10–11 [32]. The XRD analysis revealed that the lattice parameters (a and c) increased linearly with the increase in the Ca–Ba substitution.

$$L = \sqrt{\left(\frac{a^2}{3} + \left(\frac{1}{2} - U\right)^2 C^2\right)}, \tag{10}$$

$$\text{where } U = \frac{a^2}{3C^2} + 0.25. \tag{11}$$

The variation in the bond length for the entire composition is listed in Table 2 and exhibits the increasing trend with the substitution. It is well known that fundamental vibrational frequency and force constants (K_o and K_t) decrease with the increase in the bond length. So, the observed shift in the band frequency toward the lower side and reduction of the force constant K_o and k_t is due to the increase in the lattice parameters. Therefore, FTIR results are in agreement with phase identification analysis.

3.4 Dielectric measurement

Room temperature dielectric measurement was inspected in the 1–3 GHz frequency range. Dielectric measurement includes the dielectric constant, dielectric loss, tan loss factor, and Ac conductivity, suggesting valuable information regarding the electric charge carriers, which supports the conduction mechanism. These parameters are investigated as the function of frequency and the Ca–Ba proportions.

3.4.1 Dielectric constant

The dielectric constant decides the capacity of the material to store the charges when utilized in capacitors. Figure 5 shows the dependence of the dielectric constant on the frequency and compositional variation of the entire composition. It can be examined that the dielectric constant
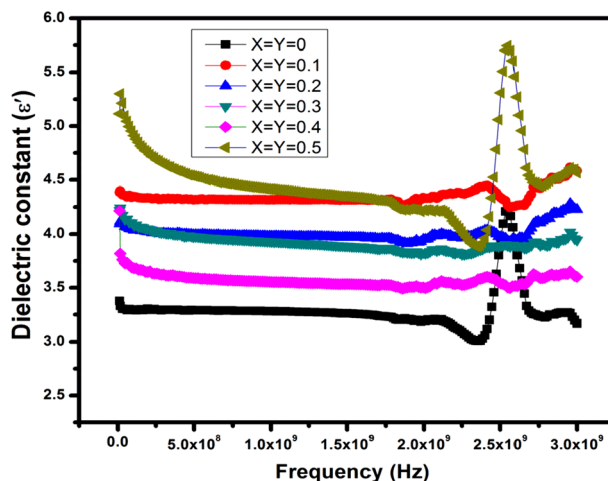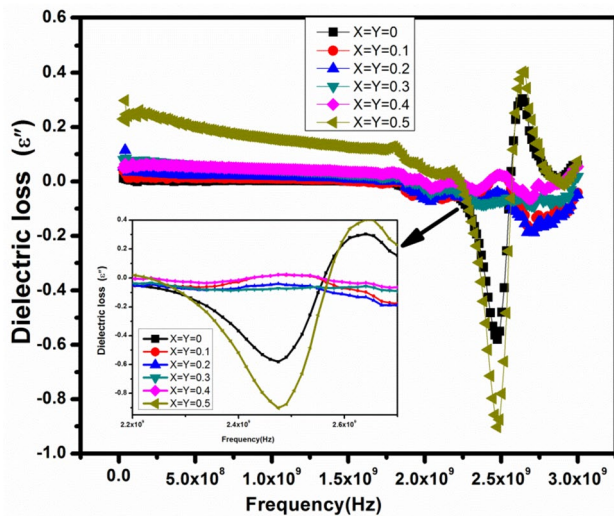

Fig. 5 The variation of dielectric constant versus frequency of $Sr_{2-x}Ca_xNi_{2-y}Ba_yFe_{28}O_{46}$ ($x=y=0$, 0.1, 0.2, 0.3, 0.4, 0.5) X-type hexaferrites

decreases with an increase in frequency, thus showing the usual behavior of the ferrites [33]. In the low-frequency region, the dielectric constant is high and decreases with further enhancement in the frequency. In contrast, the dielectric becomes independent of the frequency in the intermediate frequency region. A 2.3–2.5 resonance peak appeared at the frequency range, which is caused by the effect of hopping frequency matching of $Fe^{3+} \leftrightarrow Fe^{2+}$ ions becoming equal to the applied frequency [34].

The compositional variation with the substitution on the dielectric constant is shown in the inset graph in Fig. 5. It can be noticed from Table 4 that by varying the Ca–Ba ratio, the dielectric constant increases. At $x=y=0.5$ highest dielectric constant value was observed, i.e., 5.115. It had been reported that Ca–Ba is either distributed on A–B sites [35]. An increase in the Ca–Ba concentration on the A site enhances the dielectric constant. The optimization in dielectric parameters is referred to the Iwauchi hypothesis. The octahedral site contains many Fe^{2+} ions, and an increase in the electronic transfer among Fe^{2+} and Fe^{3+} results in the high value of the dielectric constant [36]. Nanomaterials

Table 4 Dielectric studies results of $Sr_{2-x}Ca_xNi_{2-y}Ba_yFe_{28}O_{46}$

Ca–Ba content	Dielectric constants		$tan\delta$	$\sigma_{ac}\ (\Omega cm)^{-1}$	M′	M″	n
	ε'	ε''					
$x=0, y=0$	3.376	0.0454	0.0124	1.453×10^{-5}	0.3036	0.00355	0.94
$x=0.1, y=0.1$	4.386	0.0488	0.0096	1.272×10^{-5}	0.2295	0.00218	0.54
$x=0.2, y=0.2$	4.096	0.1149	0.0235	3.822×10^{-5}	0.2470	0.00469	0.36
$x=0.3, y=0.3$	4.220	0.0687	0.01528	3.255×10^{-5}	0.2425	0.00391	0.56
$x=0.4, y=0.4$	4.215	0.0634	0.0166	1.562×10^{-5}	0.2659	0.0045	0.64
$x=0.5, y=0.5$	5.115	0,2981	0.0447	7.048×10^{-5}	0.1841	0.1003	0.56

Fig. 6 The variation of dielectric loss versus frequency of $Sr_{2-x}Ca_xNi_{2-y}Ba_yFe_{28}O_{46}$ ($x=y=0$, 0.1, 0.2, 0.3, 0.4, 0.5) X-type hexaferrites

Fig. 7 The variation of Tan loss versus frequency of $Sr_{2-x}Ca_xNi_{2-y}Ba_yFe_{28}O_{46}$ ($x=y=0$, 0.1, 0.2, 0.3, 0.4, 0.5) X-type hexaferrites

may miniaturize the microwave devices with a high dielectric constants value.

3.4.2 Dielectric loss

Figure 6 illustrates the dielectric loss factor as a function of frequency of the Ca–Ba-substituted $Sr_{1-x}Ca_xNi_{2-y}Ba_yFe_{28}O_{46}$ ($x=y=0$, 0.1, 0.2, 0.3, 0.4, 0.5) at the room temperature. The reduction in dielectric loss factor is examined by the increase in frequency owing to the similar fact as enlightened for dielectric constant [37]. From Fig. 6, it can be observed that at low frequency, the dielectric loss has a high value due to dislocations and other defects. Resonance peaks are detected at the high frequency, ascribed to the hopping mechanism [38]. It can be viewed from the inset graph that the value of the dielectric loss shows increasing behavior with the enhancement in the Ca–Ba concentration, which in turn supports the EMI shielding efficiency. This increase in the dielectric loss is attributed to the interfacial polarization and is listed in Table 4.

3.4.3 Tangent loss

Tangent loss is described as the ratio of resistive current and the charging current as given in the following relation.

$$Tan\delta = \varepsilon''/\varepsilon'. \tag{12}$$

The frequency and compositional dependence of loss tangent *(tan)* for $Sr_{2-x}Ca_xNi_{2-y}Ba_yFe_{28}O_{46}$ are illustrated in Fig. 7. The tangent loss value depends on the different reasons such as structural homogeneity, sintering conditions, the density of the charge carriers, Fe^{+2} contents, and the choice of the composition [39]. The graph shows that tan loss decreases with the increase in frequency, and resonance peaks are also observed at the higher frequency. The resonance in the tanδ spectrum is attributed to the applied field. It can be noticed from the graph that with an increase in the substitution of Ca–Ba, the tangent loss increases. This fact is justified based on the dielectric loss because ε'' is directly proportional to tan loss (δ).
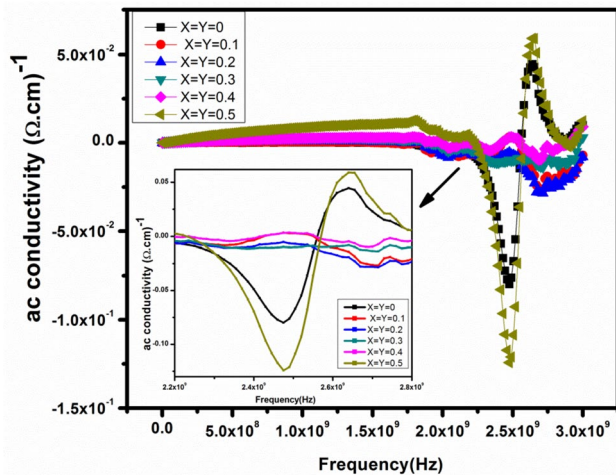
Fig. 8 The variation of Ac conductivity versus frequency of $Sr_{2-x}Ca_xNi_{2-y}Ba_yFe_{28}O_{46}$ ($x=y=0$, 0.1, 0.2, 0.3, 0.4, 0.5) X-type hexaferrites

Fig. 9 The variation of Log (Ac conductivity) versus Log (frequency) of $Sr_{2-x}Ca_xNi_{2-y}Ba_yFe_{28}O_{46}$ ($x=y=0$, 0.1, 0.2, 0.3, 0.4, 0.5) X-type hexaferrites

3.4.4 Ac conductivity

Ac conductivity can be found from the values of dielectric loss and dielectric permittivity as [40]

$$\sigma_{ac} = \varepsilon_0 \varepsilon' \omega \tan \delta. \tag{13}$$

Figure 8 demonstrates the discrepancy in the ac conductivity with frequency, and the inset graph shows the compositional dependence of the synthesized material. The variation in the ac conductivity can be clarified in terms of low- and high-frequency regions. In the low-frequency region, the probability density of charge carriers is less, while conducting grains are found more active in the high-frequency regions. This conduction is similar to Koop's theory/Maxwell–Wagner [41], i.e., the ferrite material contains conducting grains separated through highly resistive thin layers, i.e., grain boundaries [42]. According to this model, at low frequency, the ac conductivity explains the contribution of the grain boundaries.

In contrast, at high frequency, the dispersion is attributed to the conductivity of grains. The Ac conductivity reveals increasing behavior as the Ca–Ba substitution ratio increases. The increase in the ac conductivity is attributed to the decrease in the porosity [43].

For the conduction mechanism value of 'n' plays a significant role. In the current work, exponential n is determined from $\log \sigma_{ac}$ versus $\log \omega$ graph as illustrated in Fig. 9. The values of n are found in the range of 0–1. In this study, the hopping conduction is confirmed as the variation of "n" is obtained in 0.94–0.36.
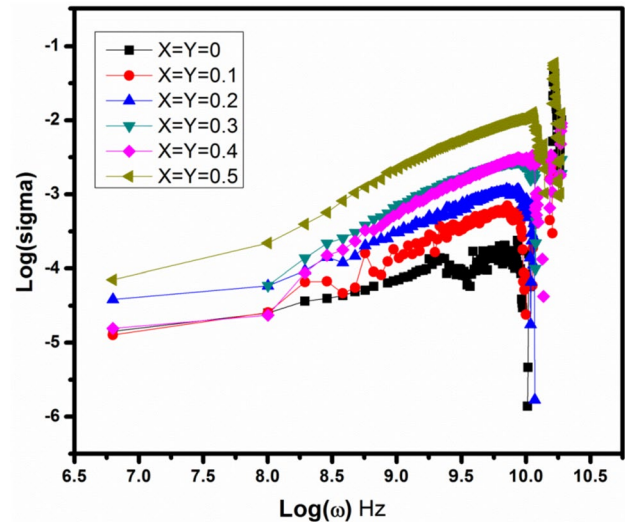
3.4.5 Quality factor

The variation in Q value of entire composition versus frequency for $Sr_{2-x}Ca_xNi_{2-y}Ba_yFe_{28}O_{46}$ ($x=y=0$–0.5) X-type hexaferrites is shown in the Fig. 10. In the current study, un-doped material shows a high resonance peak Q value at 1.5 GHz. With the increase in the Ca–Ba concentration, the resonance peak shifted in the direction of the high-frequency range of 1.5–3 GHz. This behavior can be elucidated in the presence of the pores in the prepared material. It was observed from the XRD results that by varying the doping concentration, the porosity decreases, so the Q value increase, which suggests this synthesized composition to be utilized for several electronic devices.

It has been reported that good dielectric material is the one that has a high dielectric constant and high value of the quality factor (Q x f). So this synthesized material can be regarded as good dielectric material and good material for microwave application [44].

3.4.6 Complex modulus

Complex modulus investigation is used to study the electrical transference mechanism, such as conductivity relaxation of the ceramic materials. Analysis of the dependence of the electric modulus on frequency is one of the excellent methods to recognize the relaxation time of the materials. The real (M′) and imaginary (M″) parts of the complex modulus are shown in Fig. 11–12.

Figure 11 represents the variation in M′ versus frequency for all synthesized material. It can be observed that the value of M′ is less in the low-frequency region. But further, as
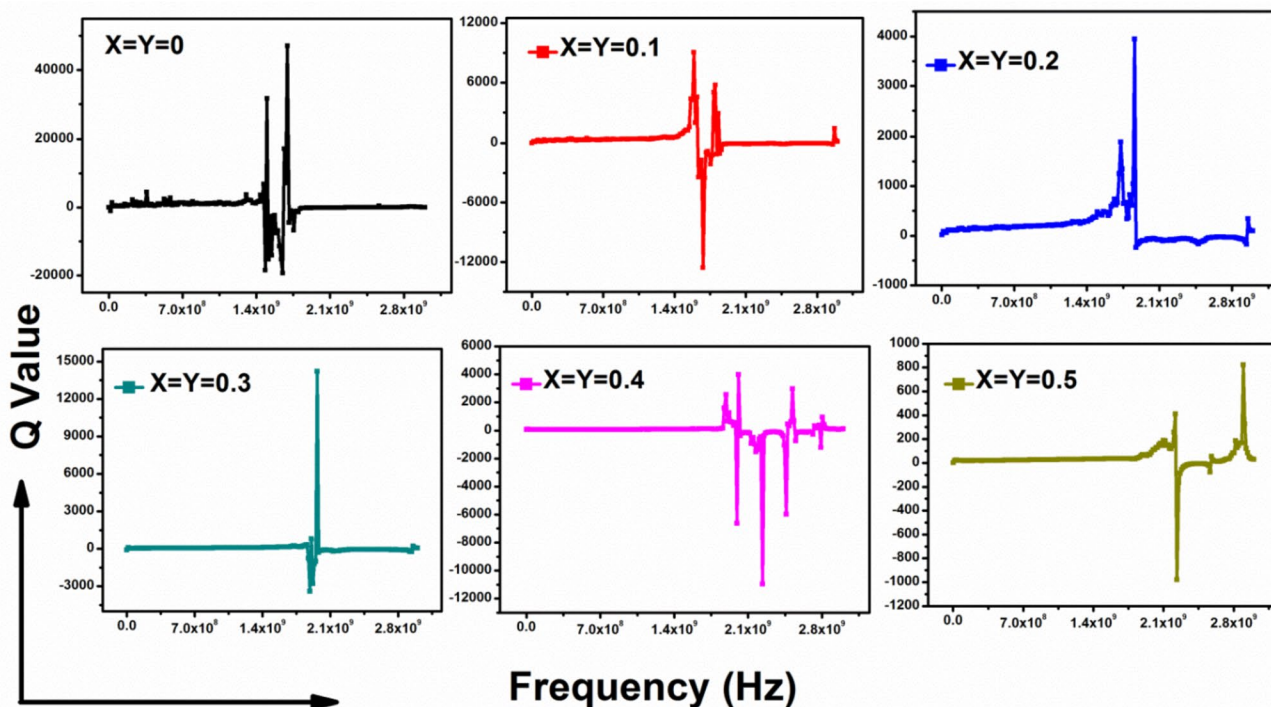
Fig. 10 The variation of Q values versus frequency of $Sr_{2-x}Ca_xNi_{2-y}Ba_yFe_{28}O_{46}$ ($x=y=0$, 0.1, 0.2, 0.3, 0.4, 0.5) X-type hexaferrites
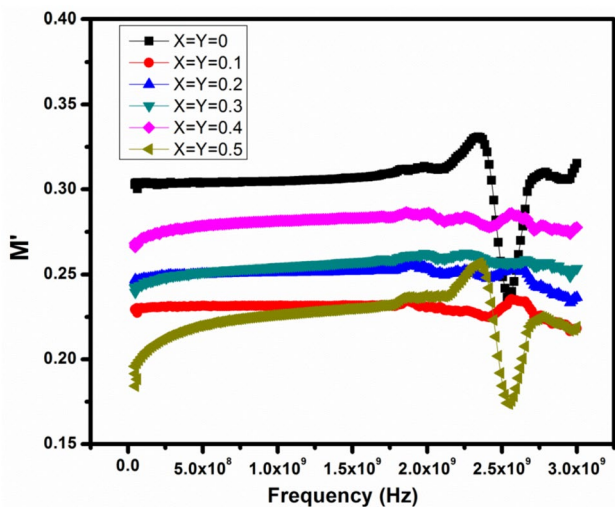

Fig. 11 The variation in real part of electric modulus (M′) versus frequency of $Sr_{2-x}Ca_xNi_{2-y}Ba_yFe_{28}O_{46}$ X-type hexaferrites
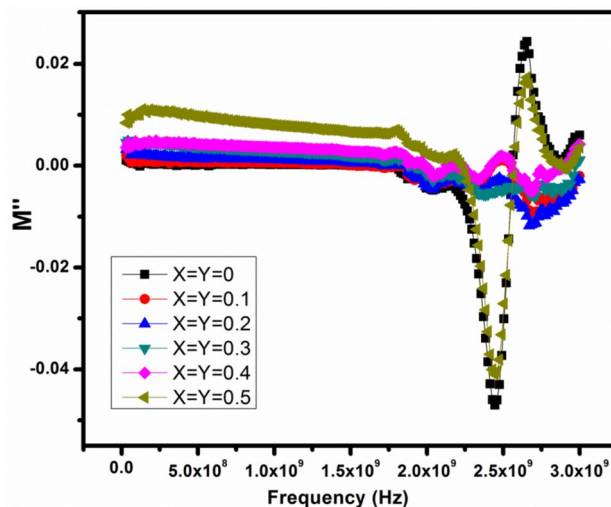
Fig. 12 The variation in imaginary part of electric modulus (M″) versus frequency of $Sr_{2-x}Ca_xNi_{2-y}Ba_yFe_{28}O_{46}$ X-type hexaferrites

the frequency increases, M′ increases and attain its maximum value and then become constant up to the frequency of 2.4 GHz. This proposed that the conduction mechanism reveals short-range mobility of the charge carriers [45].

Figure 12 shows the imaginary part of the electric modulus with the frequency. This part reveals wider information relating to the charge transport evolution like

conductivity relaxation and electrical transport mechanism as a function of frequency. It is noticed that by varying the substitution of dopants, the resonance peaks in the M″ shift toward the lower frequency. This shifting in the resonance peak is due to the resistance of grain boundaries [46]. The occurrence of the peak in the modulus spectrum

is evidence of conductivity relaxation [47]. The maximum in M″ occurs when Eq. 14 is fulfilled [48].

$$2\pi f_{max} * \tau = 1. \tag{14}$$

3.4.7 Cole–Cole plots

To investigate the contribution of the grain boundaries and grain Cole–Cole plots are plotted. It provides good information about the feasible relationship between the performance of the grain boundaries and peak happening in a complex modulus spectrum. The Cole–Cole plot of prepared composition is illustrated in Fig. 13 reveals a single semicircle and confirms deviation in their radius. The discrepancy in semicircle radius indicates the noticeable consequence of substitution. Single semicircles were noticed for the entire composition approves the liability of the grain boundaries in the conduction mechanism. The low-frequency side such that the left region of the semicircle is an effect of grain resistance [49], the intermediate frequency region below the curve indicates grain boundaries involvement, and the high-frequency region signifies the effect of both grain and grain boundaries [50].

3.5 Magnetic properties

The room temperature magnetic behavior of $Sr_{2-x}Ca_xNi_{2-y}Ba_yFe_{28}O_{46}$ ($x = y = 0–0.5$) X-type hexagonal ferrites is investigated with the maximum applied field of 30KOe. The resulting M–H loops of all prepared compositions are presented in Fig. 14. The coercivity (H_c), saturation magnetization (M_s), remanence (M_r), squareness ratio (SQR), and magnetic moment (μ_B) were calculated from the M–H loops (Table 5).

3.5.1 Saturation magnetization and remanence

Figure 15 (A and B) illustrates the effect of the Ca–Ba substitution on saturation magnetization (M_s) and remanent magnetization (M_r). It is apparent from the figure that the values of both M_s and M_r decrease with Ca–Ba contents and is tabulated in Table 5. The distinguished magnetic parameters can be described according to the cationic distribution in R and S blocks. The value of the M_r and M_s is found to be decreased by increasing Ca–Ba into proportion. These variations may be correlated to superexchange interaction among tetrahedral ($6c_{1v}$) and octahedral ($3a_{v1}$) sites of the s-blocks [51]. The replacing of Sr^{2+} ions by Ca^{2+} ions and Ni^{2+} ions by Ba^{2+} in $Sr_{2-x}Ca_xNi_{2-y}Ba_yFe_{28}O_{46}$ causes the reduction in the magnetic interactions. The decrease in the magnetic interaction is owed to the distinction in the magnetic moment of host Sr^{2+}(2.7 μB) [52]- Ni^{2+} (2 μB) [53] by substitution Ca^{2+}(1 μB) [54]–Ba^{2+}(2.3 μB) [55] ions. This discrepancy in magnetic moment signifies the decrement of the A–B superexchange magnetic interactions; consequently, M_s and M_r decreased.
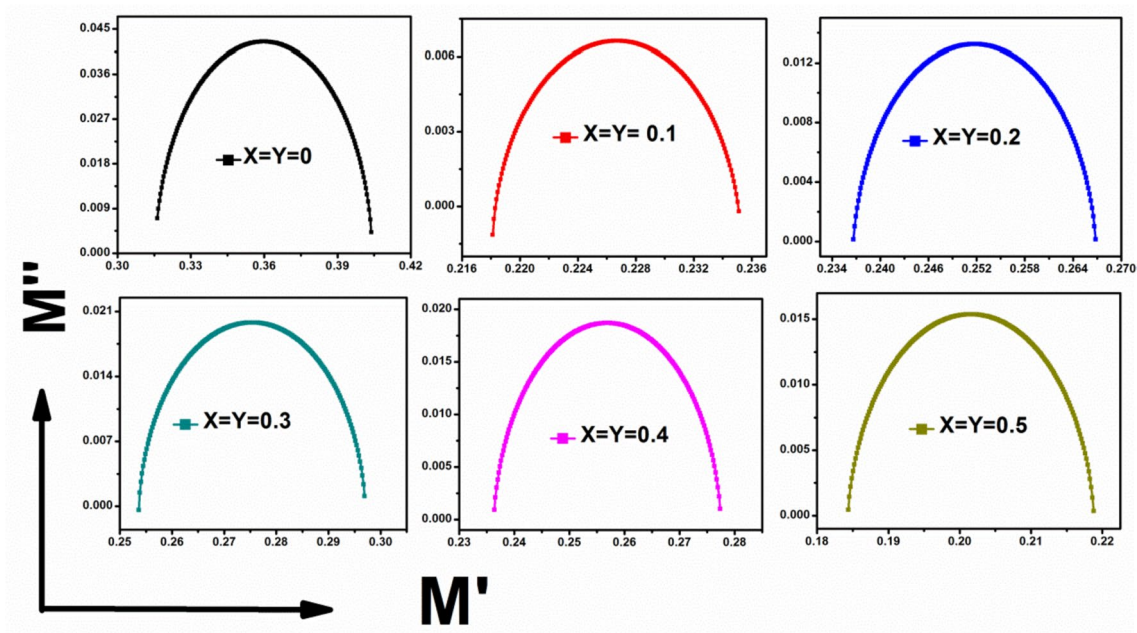

Fig. 13 Cole–Cole plots of substituted $Sr_{2-x}Ca_xNi_{2-y}Ba_yFe_{28}O_{46}$ X-type hexaferrites

Fig. 14 Magnetic hysteresis loops of $Sr_{2-x}Ca_xNi_{2-y}Ba_yFe_{28}O_{46}$ X-type hexaferrites
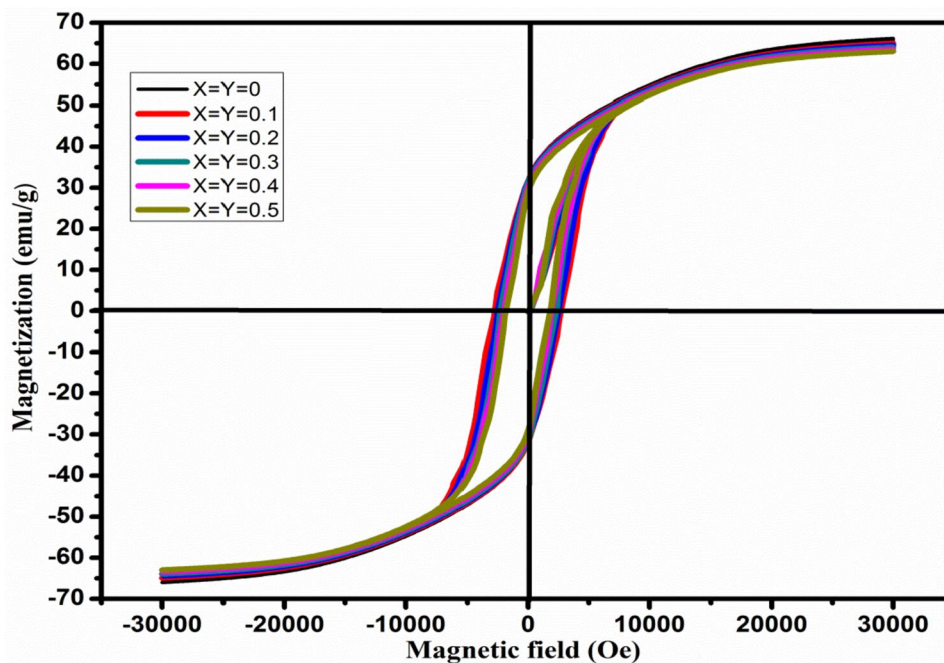
Table 5 Magnetic parameters of $Sr_{2-x}Ca_xNi_{2-y}Ba_yFe_{28}O_{46}$ (x = y = 0–0.5) X-type ferrites

Ca–Ba content	M_s (emu/g)	M_r (emu/g)	H_c (Oe)	M_r/M_s	n_B (μ_B)	K(erg/cm^3)
X = 0, Y = 0	66.2	31.4443	2506.01	0.47499	30.726	1.728 X 10^5
X = 0.1, Y = 0.1	64.9	31.6082	2683.43	0.48703	30.159	1.814 X 10^5
X = 0.2, Y = 0.2	64.5	31.4985	2493.81	0.48835	30.009	1.675 X 10^5
X = 0.3 Y = 0.3	63.8	31.39	2308.43	0.49201	29.718	1.534 X 10^5
X = 0.4, Y = 0.4	63.5	30.0466	1943.12	0.47317	29.614	1.285 X 10^5
X = 0.5, Y = 0.5	63	29.1521	1838.69	0.46273	29.416	1.206 X 10^5

3.5.2 Coercivity

Coercivity is the principle parameter used to decide the materials hard and soft magnetic nature. In the present work, the coercivity illustrates decreasing behavior with the addition of Ca–Ba additives for all samples except for x = y = 0.1, i.e., 2683.43Oe shown in Fig. 15(C). The detected values H_c varied between 2506.01 and 1838.69 Oe. This reduction in H_c can be enlightened based on grain size. It can be seen from the data for larger particles, there is a decrease in coercivity; H_c varies inversely with grain size, which is consistent in the present work. Due to smaller coercivity values, these synthesized materials can be considered best to be utilized in switching devices. In the existing study $H_c > M_r/2$, the synthesized series is regarded as excellent for their use in high-frequency operating devices [51]. Variations in the Ms and Mr are shown in Fig. 15.

3.5.3 Squareness ratio (S = Mr/Ms)

The ratio M_r/M_s is called as squareness ratio, which decides the hardness of the material and determines the inter-grain group exchanges that vary from 0 to 1. The calculated squareness ratio of the entire composition is listed in Table 5 and is found to be below 0.5, which illustrates the single domain nature of the synthesized nanoparticles.

3.5.4 Anisotropy constant (K) and magneton number (n_B)

The discrepancy in the anisotropy constant and magneton number for the entire composition were computed using the relation (Eq. 15–16) [56] and given in Table 5.
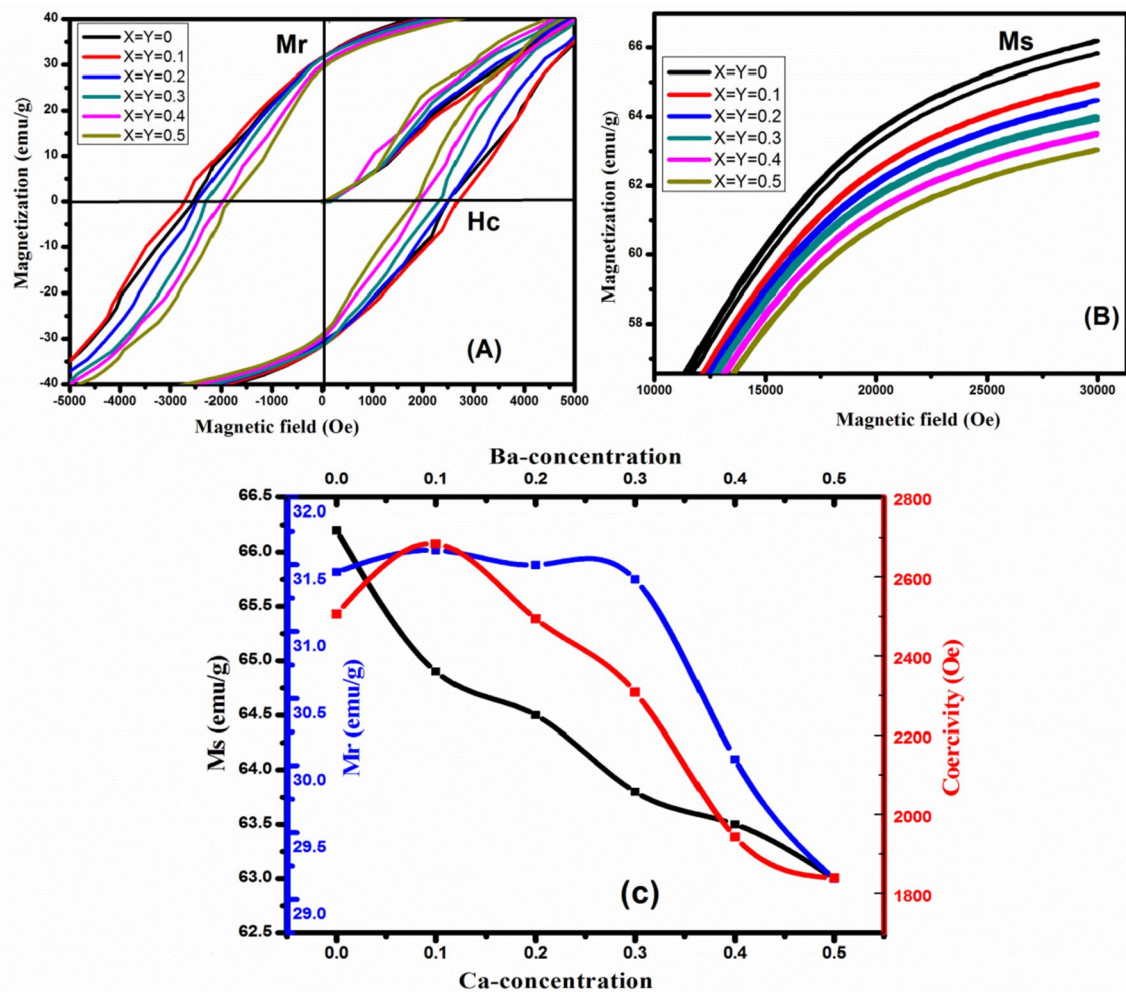
$$K = Ms * Hc / 0.96, \tag{15}$$

Fig. 15 Variation in magnetic parameters (M_s, M_r and H_c) of $Sr_{2-x}Ca_xNi_{2-y}Ba_yFe_{28}O_{46}$ X-type hexaferrites

$$n_B = M_s * M/5585. \tag{16}$$

An increase in the Ca–Ba concentration, anisotropy constant (K), and magneton number (n_B) illustrates the analogous behavior similar to that of M_s. The magnetic characteristics were influenced by Ca–Ba substitution in the SrNi based X-type hexagonal ferrite structure.

4 Conclusion

$Sr_{2-x}Ca_xNi_{2-y}Ba_yFe_{28}O_{46}$ ($x = y = 0$–0.5) X-type hexagonal ferrites were successfully synthesized via sol–gel auto-combustion route and examined the influence of Ca–Ba on the structural, spectral, dielectric parameters and the magnetic properties. Investigation concludes that with the increase of the Ca–Ba substitution, the lattice parameters, X-ray density, bulk density was found to be increased and were attributed to the higher radii ions replacement. FTIR

spectra revealed the variation in the characteristic's bands of Fe–O in tetrahedral/Octa sites towards the lower frequency side. The decrease in the fundamental vibrational frequency and force constants reveals the increase in the bond length—the Ac conductivity increases by the increasing ratios of the substituted ions. The higher values of the dielectric parameters suggest this composition is valuable for the manufacture of the multilayer chip inductor, security, sensing, and a resonant circuit. Significant variations in the magnetic parameters were observed. The magnetic investigation revealed the impact of Ca–Ba cations on the SrNi-X-type hexagonal ferrites. The decrease in M_s, M_r, and H_c proposed using this material in the high-frequency application by altering the Ca–Ba ratio. The distinguishing characteristics of this synthesized composition indicate the excellent scope in the density recording media, microwave absorber, and security applications.

Declarations

Conflict of interest The authors declare that they have no conflict of interest.

References

1. I. Ali et al., Effect of Tb–Mn substitution on DC and AC conductivity of Y-type hexagonal ferrite. J. Alloy. Compd. **579**, 576–582 (2013)
2. N. Yasmin et al., Structural and magnetic studies of Ce-Zn doped M-type SrFe12O19 hexagonal ferrite synthesized by sol-gel auto-combustion method. Ceram. Int. **45**(1), 462–467 (2019)
3. Z. Haijun, Y. Xi, Z. Liangying, The preparation and microwave properties of Ba2ZnxCo2−xFe28O46 hexaferrites. J. Magn. Magn. Mater. **241**(2), 441–446 (2002)
4. A. Majeed et al., Structural, microwave permittivity, and complex impedance studies of cation (Cr, Bi, Al, In) substituted SrNi-X hexagonal nano-sized ferrites. Ceram Intern. **46**(2), 1907–1915 (2019)
5. M. Ahmad et al., Synthesis and characterization of Al-substituted W-type hexagonal ferrites for high frequency applications. J. Alloy. Compd. **577**, 382–388 (2013)
6. B.X. Gu, Magnetic properties of X-type Ba2Me2Fe28O46 (Me=Fe Co, and Mn) hexagonal ferrites. J. Appl. Phys. **71**(10), 5103–5106 (1992)
7. M.Y. Lodhi et al., Role of Nd-Ni on structural, spectral and dielectric properties of strontium-barium based nano-sized X-type ferrites. Ceram. Int. **44**(3), 2968–2975 (2018)
8. A. Majeed et al., Influence of Cr and Zn substitution on structural, magnetic and dielectric properties of Sr2-xZnxNi2Fe28-yCryO46 X-type hexagonal ferrite. Solid State Sci. **100**, 106090 (2020)
9. A. Majeed et al., Structural elucidation and magnetic behavior evaluation of rare earth (La, Nd, Gd, Tb, Dy) doped BaCoNi-X hexagonal nano-sized ferrites. J. Magn. Magn. Mater. **408**, 147–151 (2016)
10. R.C. Pullar, Hexagonal ferrites: a review of the synthesis, properties and applications of hexaferrite ceramics. Prog. Mater Sci. **57**(7), 1191–1334 (2012)
11. K. Rana et al., Investigation of cobalt substituted M-type barium ferrite synthesized via Co-precipitation Method for Radar Absorbing Material in Ku-band (12–18GHz). Ceram Intern. **44**(6), 6370–6375 (2018)
12. R.C. Pullar, A.K. Bhattacharya, The synthesis and characterisation of Co2X (Ba2Co2Fe28O46) and Co2U (Ba4Co2Fe36O60) ferrite fibres, manufactured from a sol-gel process. J. Mater. Sci. **36**(19), 4805–4812 (2001)
13. Z. Haijun et al., Dielectric and magnetic properties of ZnCo-substituted X hexaferrites prepared by citrate sol–gel process. Mater. Res. Bull. **38**(2), 363–372 (2003)
14. V. Harikrishnan et al., Effect of annealing temperature on the structural and magnetic properties of CTAB-capped SrFe12O19 platelets. J. Magn. Magn. Mater. **401**, 775–783 (2016)
15. S.R. Ejaz et al., Structural, spectral, dielectric and magnetic properties of Co–Cr-substituted hexagonal ferrites with X-type structure. J Korean Ceram Soc. **20**, 1–12 (2022)
16. S.U. Asif et al., Effect of Dy-Co on physical and magnetic properties of X-type hexaferrites (Ba2−xDyxCu2Fe28−yCoyO46). Chin. J. Phys. **61**, 47–54 (2019)
17. M. Ahmad et al., Effects of Sr-substitution on the structural and magnetic behavior of Ba-based Y-type hexagonal ferrites. J. Alloy. Compd. **580**, 23–28 (2013)
18. M.J. Iqbal, F. Liaqat, Physical and electrical properties of nano-sized Mn-and Cr-doped strontium Y-type hexagonal ferrites. J. Am. Ceram. Soc. **93**(2), 474–480 (2010)
19. M.Y. Lodhi et al., Structural, magnetic and dielectric properties of Dy-Co substituted Sr-Ba-Mg-based magnetic oxides. Appl. Phys. A **127**(11), 872 (2021)
20. M. Hakimi, P. Alimard, Fabrication and properties of Nd-La doped Sr2CuMgFe28O46 nanoparticles anchored with sheets of reduced graphene oxide. Ceram. Int. **40**(9), 14501–14507 (2014)
21. I. Sadiq et al., Nanosized Ce–Zn substituted microwave absorber material for X-band applications. J. Magn. Magn. Mater. **370**, 25–31 (2014)
22. M. Ahmad et al., Structural, physical, magnetic and electrical properties of La-substituted W-type hexagonal ferrites. Ceram. Int. **37**(8), 3691–3696 (2011)
23. M.A. Khan et al., Structural, magnetic and dielectric properties of Yb3+ doped BaCo-X hexagonal nanoferrites. J. Alloy. Compd. **695**, 3674–3681 (2017)
24. X. Huang et al., Microstructure and magnetic properties of Ca-substituted M-type SrLaCo hexagonal ferrites. J. Magn. Magn. Mater. **378**, 424–428 (2015)
25. H. Zheng et al., Magnetic properties of hexagonal barium ferrite films on Pt/MgO (111) substrates annealed at different temperatures. J. Magn. Magn. Mater. **413**, 25–29 (2016)
26. A. Manzoor et al., Tuning magnetic and high frequency dielectric behavior in Li-Zn ferrites by Ho doping. Ceram. Int. **44**(6), 6321–6329 (2018)
27. C.V. Reddy et al., Effect of calcination temperature on cobalt substituted cadmium ferrite nanoparticles. J. Mater. Sci. Mater. Electron. **26**(7), 5078–5084 (2015)
28. S. El-Sayed et al., Effect of trivalent ion substitution on the physical properties of M-type hexagonal ferrites. Part. Sci. Technol. **32**(1), 39–45 (2014)
29. Z. Mosleh et al., Structural, magnetic and microwave absorption properties of Ce-doped barium hexaferrite. J. Magn. Magn. Mater. **397**, 101–107 (2016)
30. Y. Zhou et al., Photo-Fenton degradation of ammonia via a manganese–iron double-active component catalyst of graphene–manganese ferrite under visible light. Chem. Eng. J. **283**, 266–275 (2016)
31. S. El-Sayed et al., Magnetic behavior and dielectric properties of aluminum substituted M-type barium hexaferrite. Physica B **426**, 137–143 (2013)
32. A. Sahai, N. Goswami, Structural and vibrational properties of ZnO nanoparticles synthesized by the chemical precipitation method. Physica E **58**, 130–137 (2014)
33. M.J. Iqbal, M.N. Ashiq, Physical and electrical properties of Zr–Cu substituted strontium hexaferrite nanoparticles synthesized by co-precipitation method. Chem. Eng. J. **136**(2–3), 383–389 (2008)
34. S. Shakoor et al., Electrical, dielectric and magnetic characterization of Bi–Cr substituted M-type strontium hexaferrite nanomaterials. J. Magn. Magn. Mater. **362**, 110–114 (2014)
35. S. Assar, H. Abosheiasha, Effect of Ca substitution on some physical properties of nano-structured and bulk Ni-ferrite samples. J. Magn. Magn. Mater. **374**, 264–272 (2015)
36. M.N. Ashiq et al., Structural, electrical, dielectric and magnetic properties of Gd-Sn substituted Sr-hexaferrite synthesized by sol–gel combustion method. J. Magn. Magn. Mater. **374**, 173–178 (2015)
37. K. Chandra Babu Naidu, W. Madhuri, Microwave processed bulk and nano NiMg ferrites: a comparative study on X-band electromagnetic interference shielding properties. Mater Chem Phy. **187**, 164–176 (2017)
38. L.-Z. Li et al., Structural, magnetic and electrical properties of Zr-substitued NiZnCo ferrite nanopowders. J. Magn. Magn. Mater. **435**, 58–63 (2017)

39. C.C. Chauhan et al., Structural, magnetic and dielectric properties of Co-Zr substituted M-type calcium hexagonal ferrite nanoparticles in the presence of α-Fe_2O_3 phase. Ceram Intern. **44**(15), 17812–17823 (2018)

40. S. Mahalakshmi, K. SrinivasaManja, S. Nithiyanantham, Electrical properties of nanophase ferrites doped with rare earth ions. J. Supercond. Novel Magn. **27**(9), 2083–2088 (2014)

41. C. Ramana et al., Correlation between structural, magnetic, and dielectric properties of manganese substituted cobalt ferrite. J. Appl. Phys. **114**(18), 183907 (2013)

42. M. Irfan et al., Influence of Nd 3+ substitution on physical, electrical and dielectric properties of $Ba_2 Zn_2 Fe_{12} O_{22}$ hexagonal ferrites prepared by sol–gel auto combustion method. J. Mater. Sci.: Mater. Electron. **27**(4), 3637–3644 (2016)

43. E. Pervaiz, I. Gul, Structural, electrical and magnetic studies of Gd3+ doped cobalt ferrite nanoparticles. Intern J Curr Eng Technol **2**(4), 377–387 (2012)

44. N. Chandamma et al., Structural and electrical properties of Zinc doped Nickel ferrites nanoparticles prepared via facile combustion technique. J. Alloy. Compd. **702**, 479–488 (2017)

45. B. Chowdari, R. Gopalakrishnan, AC conductivity analysis of glassy silver iodomolybdate system. Solid State Ionics **23**(3), 225–233 (1987)

46. A. Manzoor et al., Investigation of structural, dielectric and magnetic properties of Ho substituted nanostructured lithium ferrites synthesized via auto-citric combustion route. J. Alloy. Compd. **710**, 547–556 (2017)

47. M.M. Costa, G.F.M. Pires Júnior, A.S.B. Sombra, Dielectric and impedance properties' studies of the of lead doped (PbO)-Co_2Y type hexaferrite ($Ba_2Co_2Fe_{12}O_{22}$ (Co_2Y)). Mater Chem Phy. **123**(1), 35–39 (2010)

48. M. Costa, G.P. Junior, A. Sombra, Dielectric and impedance properties' studies of the of lead doped (PbO)-Co_2Y type hexaferrite ($Ba_2Co_2Fe_{12}O_{22}$ (Co_2Y)). Mater. Chem. Phys. **123**(1), 35–39 (2010)

49. Y. Bai et al., Complex Y-type hexagonal ferrites: an ideal material for high-frequency chip magnetic components. J. Magn. Magn. Mater. **264**(1), 44–49 (2003)

50. Y. Bai et al., Electrical properties of non-stoichiometric Y-type hexagonal ferrite. J. Magn. Magn. Mater. **278**(1–2), 208–213 (2004)

51. M.A. Khan et al., Structural, spectral, dielectric and magnetic properties of Sr_2CuxNi_2-xFe_{28}-$xCrxO_{46}$ ($0 \leq x \geq 0.5$) ferrites synthesized via micro-emulsion route. Mater Chem Phy. **259**, 124066 (2021)

52. S. Anjum et al., Effect of strontium doped M-Type bariam hexaferrites on structural, magnetic and optical properties. Optik **131**, 977–985 (2017)

53. P. Kaur, S. Bahel, S.B. Narang, Microwave absorption behavior and electromagnetic properties of Ni-Zr doped La-Sr hexagonal ferrite synthesized by auto-combustion method. Mater. Res. Bull. **100**, 275–281 (2018)

54. Y. Yang et al., Influence of calcium content on the structural and magnetic properties of Sr0.70−xCaxLa0.30Fe11.75Zn0.25O19 hexagonal ferrites. J Magn Magn Mater. **401**, 1039–1045 (2016)

55. S.R. Ejaz et al., Study of structural transformation and hysteresis behavior of Mg-Sr substituted X-type hexaferrites. Ceram. Int. **44**(15), 18903–18912 (2018)

56. Au. Rehman et al., Evaluations of structural, magnetic and various dielectric parameters of Ni-substituted Zn_2W-type hexagonal ferrites for high frequency (1–6 GHz) applications. Ceram Intern. **45**(18), 24202–24211 (2019)